A. Frezzotti, P. Barbante, L. Gibelli
Direct Simulation Monte Carlo Applications to Liquid-Vapor Flows
Physics of Fluids, Vol. 31, N. 6, 2019, 062103 (14 pages)
doi:10.1063/1.5097738

Direct Simulation Monte Carlo Applications to Liquid-Vapor Flows

A. Frezzotti,[1] P. Barbante,[2] and L. Gibelli[3]

[1)]*Dipartimento di Scienze & Tecnologie Aerospaziali, Politecnico di Milano*

Via La Masa, 34 - 20156 Milano, Italy[a)]

[2)]*Dipartimento di Matematica, Politecnico di Milano*

Via Bonardi, 9 - 20133 Milano, Italy[b)]

[3)]*School of Engineering, University of Edinburgh*

Robert Stevenson Road - Edinburgh EH9 3FB, UK[c)]

(Dated: 7 May 2019)

The paper aims at presenting Direct Simulation Monte Carlo (DSMC) extensions and applications to dense fluids. A succint review of past and current research topics is presented, followed by a more detailed description of DSMC simulations for the numerical solution of Enskog-Vlasov equation, applied to the study of liquid-vapor flows. Results about simulations of evaporation of a simple liquid in contact with a dense vapor are presented as an example.

[a)]Electronic mail: aldo.frezzotti@polimi.it.

[b)]Electronic mail: paolo.barbante@polimi.it.

[c)]Electronic mail: livio.gibelli@ed.ac.uk.

I. INTRODUCTION

The Direct Simulation Monte Carlo (DSMC), proposed by G. A. Bird in 1963[1] represented a real breakthrough in the field of kinetic theory[2]. In the years, DSMC made possible the numerical treatment of increasingly complex problems[3,4], governed by the Boltzmann equation or related kinetic models. The key of the success of DSMC is its elegant simplicity which allows accommodating physical gas models of growing complexity while keeping the same general scheme structure and robustness.

Although the vast majority of DSMC studies are based on dilute gas models, the flexibility of DSMC schemes makes possible extensions to dense fluids, *i.e.* fluids in which the molecular size (or the range of intermolecular forces) is comparable with the average intermolecular spacing[5]. The smaller extent of this research area reflects the more limited development of kinetic theory of dense fluids. Nevertheless, the more complex structure of kinetic models makes DSMC even more important, since it gives both theory and applications the possibility to go beyond the mere calculation of dense fluids thermodynamic and transport properties. In turn, this permits one to assess more extensively the models capabilities.

DSMC schemes for dense fluids have been developed along two distinct research lines. The first one[6,7] has been based on a direct modification of the DSMC algorithm, originating from the observation that the addition of a spatial displacement step to the particles advection and local collision steps would make the fluid non-ideal. Tuning the rules governing the particles relative displacements allows simulating fluids with different equations of state[7]. Later, the kinetic equation underlying the generalized DSMC scheme has been derived in Ref. 8. The second research line followed a different path, in that the modifications introduced into the original DSMC collision scheme were taylored on an existing kinetic equation. The latter was proposed by David Enskog in 1922[9], in an attempt to extend the Boltzmann equation to deal with dense fluids.

Although based on a simplified model of the hard sphere fluid, Enskog theory has been rather successful in predicting transport properties of simple fluids[10]. Moreover, very good agreement between molecular dynamics (MD) simulations and direct numerical solutions of Enskog equation has been found in the study of shock waves propagation in a hard sphere fluid[11]. The first particle scheme for the numerical solution of the Enskog equation was proposed in Ref. 12. The scheme implementation followed Nambu's method[13], which made easier coping with the non-local character of Enskog equation collision integral at the cost of conserving momentum and energy only

in a statistical sense[14]. True DSMC extensions for the Enskog equation have been proposed in Refs. 15 and 16.

It is interesting to note that Enskog and Enskog-like equations, as well as the associated DSMC schemes, are not only relevant to investigate fundamental aspects of statistical mechanics but they have also found application to modeling of dry granular media[17,18].

As mentioned above, Enskog theory of dense fluids is based on the hard sphere potential which limits its range af application to situations where attractive intermolecular forces can be neglected, for instance when the dense fluid temperature is well above its critical value. Hence, an extension of the theory to include attractive forces is highly desirable, both from the theoretical and practical point of view. Such an extension has been proposed by De Sobrino in 1967[19]. As described in Section II, intermolecular interaction is represented as the superposition of the hard sphere potential and an attractive smooth tail. The short-range repulsive forces are treated as in the standard or revised Enskog equation theory, while the long-range attractive forces enter the equation in the form of a mean-field Vlasov term. Accordingly, this kinetic equation is referred to as Enksog-Vlasov (EV) equation. The extension, although resulting from an approximate treatment of pair correlations, gives the model the capability of providing a unified description of both liquid and vapor phases, including the interface region[20,21]. It has been later proved that the EV equation can be derived from the Liouville equation by applying the principle of maximization of entropy[22] and it leads to Korteweg equations for non-isothermal liquid-vapour systems in the hydrodynamic limit[23]. The mathematical properties of the EV equation and of simplified version of it has been extensively studied in connection with the liquid-vapor phase transition[24–27].

In spite of its approximate nature, the EV equation can mimic the fundamental physics of the condensed state[22,28,29] and, therefore, it is a useful bridge between the continuum approaches, which fail to properly deal with the complexities of interfacial phenomena and MD simulations, which can potentially provide an accurate description but are computationally demanding. Because of the EV equation ability to describe the liquid-vapor interface, most of its applications have been devoted to determine the kinetic boundary conditions that need to be prescribed at the liquid-vapor interface[30,31]. In particular, the statistical features of atoms spontaneously emitted by the liquid bulk has been elucidated by studying the evaporation into vacuum for both simple[21,32] and binary liquids[33]. The contribution of back scattered molecular flux from the vapour to the liquid has also been extensively investigated[34,35]. Studies have also been carried out for liquid-vapor flows in confined geometries[36]. In addition to presenting the above brief review of the extensions

and applications of DSMC to dense fluids, the paper aims at giving a more detailed description of its applications to liquid-vapor flows . Accordingly, Sections II and III provide a description of Enskog-Vlasov equation and the associated DSMC scheme, respectively. Section IV describes a specific application of DSMC to the study of the evaporation of a non-ideal vapor from a liquid slab. As discussed below, this problem is not addressed in the literature in spite of its theoretical interest and potential practical relevance.

II. THE ENSKOG-VLASOV KINETIC EQUATION

Enskog-Vlasov equation[19] provides an approximate kinetic description of a fluid composed of identical molecules of mass m, interacting through a Sutherland potential ϕ in the form:

$$\phi(\rho) = \begin{cases} +\infty & \rho < \sigma \\ \phi_t(\rho) & \rho \geq \sigma \end{cases} \tag{1}$$

As shown by Eq. (1), the isotropic potential $\phi(\rho)$ depends on the distance $\rho = ||\mathbf{r}_1 - \mathbf{r}||$ between two molecules whose centers are located at $\mathbf{r}$ and $\mathbf{r}_1$, respectively. Short range repulsive molecular forces are taken into account by the hard sphere contribution to ϕ, whereas the soft potential tail $\phi_t(\rho)$ describes attractive forces, acting at distance larger than the hard sphere diameter σ.

As discussed in Refs. 19 and 22, it is possible to obtain EV equation as a closed kinetic equation for the one-particle[5] distribution function $f(\mathbf{r},\mathbf{v},t)$:

$$\frac{\partial f}{\partial t} + \mathbf{v}\cdot\nabla_{\mathbf{r}} f + \frac{\mathbf{F}_t(\mathbf{r},t)}{m}\cdot\nabla_{\mathbf{v}} f = C_{hs}(f,f)\,. \tag{2}$$

In Eq. (2), $C_{hs}(f,f)$ is a collision integral which describes impulsive binary collisions in a *dense hard sphere* fluid, according to Enskog theory[9]:

$$C_{hs}(f,f) = \sigma^2 \int_{\mathscr{S}} \left\{ \chi_{hs}(\mathbf{r},\mathbf{r}+\sigma\hat{\mathbf{k}}) f(\mathbf{r}+\sigma\hat{\mathbf{k}},\mathbf{v}_1^*,t) f(\mathbf{r},\mathbf{v}^*,t) - \right.$$
$$\left. \chi_{hs}(\mathbf{r},\mathbf{r}-\sigma\hat{\mathbf{k}}) f(\mathbf{r}-\sigma\hat{\mathbf{k}},\mathbf{v}_1,t) f(\mathbf{r},\mathbf{v},t) \right\} (\mathbf{v}_r\cdot\hat{\mathbf{k}})^+ d\mathbf{v}_1 d^2\hat{\mathbf{k}}\,. \tag{3}$$

In the above equation, $\mathbf{v}$ denotes the velocity of the center of mass of a molecule, $\hat{\mathbf{k}}$ a unit vector which assigns the relative position of two molecules at the time of their impact, whereas $(\mathbf{v}^*,\mathbf{v}_1^*)$ are pre-collision velocities transformed into $(\mathbf{v},\mathbf{v}_1)$ by a hard sphere collision, according to the following relationships:

$$\mathbf{v}^* = \mathbf{v} + \left(\mathbf{v}_r\cdot\hat{\mathbf{k}}\right)\hat{\mathbf{k}}, \tag{4}$$

$$\mathbf{v}_1^* = \mathbf{v}_1 - \left(\mathbf{v}_r\cdot\hat{\mathbf{k}}\right)\hat{\mathbf{k}}. \tag{5}$$

It is to be noted that Enskog's form of the hard sphere collision integral differs from its corresponding form in Boltzmann equation for dilute gases in two important aspects. First of all, hard sphere collision partners occupy different positions, giving rise to a non-local form of $C_{hs}(f,f)$. Second, in dense fluids the volume fraction occupied by molecules is no longer negligible. Pair spatial correlations are taken into account by the velocity independent pair correlation function at contact[5], $\chi_{hs}(\mathbf{r},\mathbf{r}\pm\sigma\hat{\mathbf{k}})$. Following the simplest formulation of Enskog theory[37], the latter has been assumed to be a function of local number density. More precisely, it has been assumed that:

$$\chi_{hs}(\mathbf{r},\mathbf{r}\pm\sigma\hat{\mathbf{k}}) = \chi_{hs}\left[n\left(\mathbf{r}\pm\sigma\frac{\hat{\mathbf{k}}}{2}\right)\right], \tag{6}$$

$$\chi_{hs}(n) = \frac{1}{2}\frac{2-\eta}{(1-\eta)^3}, \qquad \eta = \frac{\pi\sigma^3 n}{6}. \tag{7}$$

The expression given by Eq. (7) ensures that the hard sphere contribution to the EV fluid equation of state is consistent with the accurate Carnhan-Starling approximation[38].

Since pair correlations are completely neglected when considering the soft potential tail $\phi_t(\rho)$ interactions, their effect is accounted by the self-consistent force field $\mathbf{F}_t(\mathbf{r},t)$:

$$\mathbf{F}_t(\mathbf{r},t) = \int_{\rho>\sigma} \frac{d\phi_t}{d\rho}\frac{\mathbf{r}_1-\mathbf{r}}{\|\mathbf{r}_1-\mathbf{r}\|} n(\mathbf{r}_1,t)\,d\mathbf{r}_1, \tag{8}$$

which results to be a linear functional of the number density field $n(\mathbf{r},t)$.

In view of the application described in Section IV, it is convenient to give the spatially one-dimensional form of EV equation for planar geometry:

$$\frac{\partial f}{\partial t} + v_x\frac{\partial f}{\partial x} + \frac{F_x(x,t)}{m}\frac{\partial f}{\partial v_x} = C_{hs}(f,f), \tag{9}$$

being x the coordinate spanning the directions of flow gradients. Simple manipulations of Eq. (8) lead to the following form for the self-consistent force field, now represented by its single component F_x:

$$F_x(x,t) = -2\pi\left[\phi_t(\sigma)\int_{|y-x|\le\sigma}(y-x)n(y,t)\,dy + \int_{|y-x|>\sigma}(y-x)\phi_t(|y-x|)n(y,t)\,dy\right]. \tag{10}$$

A. Equilibrium solutions of EV equation

A brief description of the properties of equilibrium solutions of EV equation seems in order here, because of their relevance for the evaporation flows described in Section IV. A more complete account is given in Ref. 21.

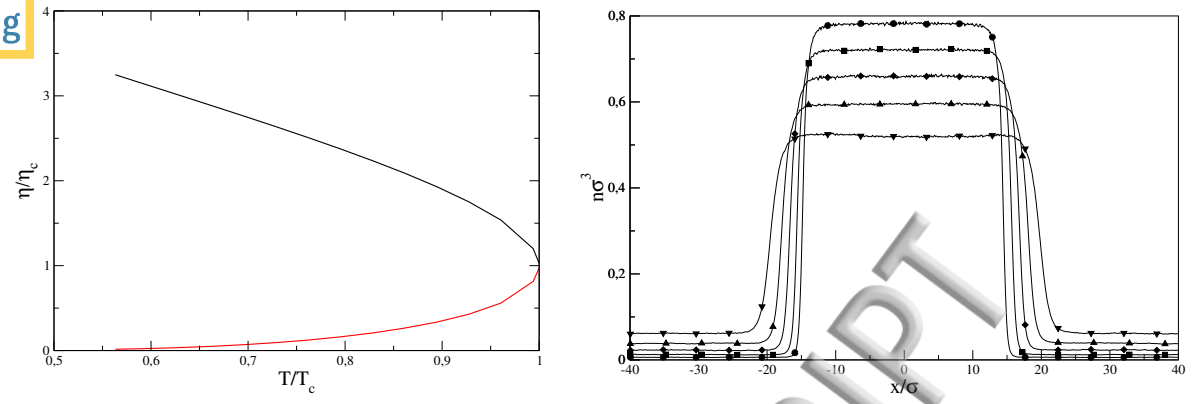

FIG. 1. **(a)**- Vapor-liquid equilibrium coexistence curve from Eq. (16). Algebraic potential tail with $\gamma = 6$. **(b)**- Equilibrium density profiles: $T/T_c = 0.596$ ($\circ$), $T/T_c = 0.663$ ($\square$), $T/T_c = 0.729$ ($\diamond$), $T/T_c = 0.795$ ($\triangle$), $T/T_c = 0.862$ ($\triangledown$). Algebraic potential tail with $\gamma = 6$.

Uniform equilibrium solutions of EV equation are characterized by Maxwellian distribution functions having constant number density n and temperature T. In uniform equilibrium, the pressure p is related to n and T by a generalized van der Waals equation of state[39]:

$$p(n,T) = p_{hs}(n,T) - \alpha_t n^2, \tag{11}$$

where $p_{hs}(n,T) = nk_BT(1+\eta+\eta^2-\eta^3)/(1-\eta)^2$ is the hard sphere pressure equation of state, consistent with the Carnahan-Starling approximation for χ_{hs}, as given by Eq. (7). The potential tail contribution to the pressure equation of state is proportional to n^2, being α_t a constant depending on ϕ_t. The particular form of the obtained equation of state causes the critical reduced density $\eta_c = \pi\sigma^3 n_c/6$ to take the value 0.1304439008, irrespective of the particular choice for ϕ_t. At variance with density, the critical temperature T_c is affected by the assumed soft potential tail form. In the case of the algebraic tail

$$\phi_t(\rho) = -\phi_\sigma \left(\frac{\sigma}{\rho}\right)^\gamma, \quad \phi_\sigma, \gamma > 0, \tag{12}$$

adopted in a number of EV equation applications[21,34], the critical temperature is related to the potential parameters by the following expression:

$$T_c^* = \frac{k_BT_c}{\phi_\sigma} = \frac{1}{\alpha_c}\frac{4\gamma}{\gamma-3}, \quad \alpha_c = 10.60122838879298. \tag{13}$$

On the other hand, considering an exponential tail in the form

$$\phi_t(\rho) = -\phi_\sigma \exp\left[-\lambda\left(\frac{\rho-\sigma}{\sigma}\right)\right], \tag{14}$$

leads to the following expression for the critical temperature:

$$T_c^* = \frac{k_B T_c}{\phi_\sigma} = \frac{4}{\alpha_c}(1 + \frac{3}{\lambda} + \frac{6}{\lambda^2} + \frac{6}{\lambda^3}). \tag{15}$$

as a function of the normalized potential decay distance λ.

If the uniform equilibrium temperature T of the fluid is lower than T_c, then EV equation admits non-uniform equilibrium solutions corresponding to a two-phase system in which liquid and vapor coexist, being separated by a smooth interface[21]. In this case, the fluid density profile obeys the equation[20,21]:

$$k_B T \frac{dn}{dx} = n(x) F_x(x) + 2\pi\sigma^2 n(x) k_B T \int_{-1}^{+1} k_x \chi_{hs}\left[n\left(x - \frac{\sigma}{2}k_x\right)\right] n(x - \sigma k_x)\, dk_x, \tag{16}$$

where F_x is given by the steady version of Eq. (10). The equilibrium liquid and vapor bulk density values, $n_l(T)$ and $n_v(T)$, that the fluid takes far from the interface, can be determined by Maxwell's equal areas rule applied to isotherms given by Eq. (11) or by equating the proper chemical potentials in the liquid and vapor phases[33]. Figure 1 shows the vapor-liquid coexistence curve obtained by setting ϕ_t as in Eq. (12), with $\gamma = 6$ to mimic the attractive contribution in the classical $12-6$ Lennard-Jones potential[40]. The same potential tail has been used to compute the equilibrium density profiles shown on the right panel of Fig. 1. Equilibrium solutions have been obtained by the DSMC extensions described in Section III.

A selected set of fluid properties, taken from the vapor-liquid coexistence curve, is presented in Table I as a function of the equilibrium temperature. The corresponding equilibrium solutions have been used as initial data in the simulations presented and discussed in Section IV. The considered equilibrium states span a temperature interval in which the vapor phase exhibits significant deviations from the ideal behavior, as indicated by the vapor compressibility $Z_v(T) = p(n,T)/(nk_BT)$ and the value of the hard sphere mean free path, normalized to hard sphere diameter, $\lambda/\sigma = 1/[\sqrt{2}\pi n\sigma^3\chi_{hs}(n)]$.

III. DSMC PARTICLE SCHEME FOR EV EQUATION

Enskog-Vlasov equation can be solved by an extension of the original DSMC scheme to dense fluids, described in Refs. 15, 21, and 36 and reported here to give a more self-contained presentation. Modifications are only required in the collision algorithm because of the non-local structure of the Enskog collision integral, the main framework of the DSMC scheme being unchanged.

TABLE I. Reduced liquid number density $n_l^* = n_l\sigma^3$, reduced vapor number density $n_v^* = n_v\sigma^3$, reduced pressure $p^* = p\sigma^3/\phi_\sigma$, vapor compressibility $Z_v(T) = p(n,T)/(nk_BT)$, and normalized hard sphere mean free path $\lambda/\sigma = 1/[\sqrt{2}\pi n\sigma^3\chi_{hs}(n)]$, as a function of reduced equilibrium temperature $T^* = k_BT/\phi_\sigma$.

T^*	T/T_c	n_l^*	n_v^*	p^*	Z_v	λ_v/σ
0.50	0.6626	0.7187	1.2213e-02	5.6822e-03	0.9237	1.7988e+01
0.55	0.7288	0.6568	2.3111e-02	1.1154e-02	0.8739	9.4004e+00
0.60	0.7951	0.5917	3.9941e-02	1.9436e-02	0.8093	5.3298e+00
0.65	0.8613	0.5205	6.5517e-02	3.1009e-02	0.7275	3.1434e+00
0.70	0.9276	0.4363	0.1066	4.6261e-02	0.6201	1.8283e+00

In particular, the one-particle distribution function $f(\mathbf{r},\mathbf{v},t)$ is represented as a superposition of N_p Dirac's δ functions

$$f(\mathbf{r},\mathbf{v},t) = \mathscr{W}\sum_{i=1}^{N_p}\delta\left(\mathbf{r}-\mathbf{r}_i(t)\right)\delta\left(\mathbf{v}-\mathbf{v}_i(t)\right), \tag{17}$$

each term $\delta\left(\mathbf{r}-\mathbf{r}_i\right)\delta\left(\mathbf{v}-\mathbf{v}_i\right)$ representing the contribution of a mathematical particle, characterized by its spatial position $\mathbf{r}_i(t)$ and velocity $\mathbf{v}_i(t)$. It should be noticed that, in general, N_p is not equal to the real number of particles present in the simulated flow field and the weight $\mathscr{W}$, equal to the ratio of the number of real to the number of simulation particles, accounts for that.

In the simulation of one or two-dimensional flow-fields, the number of computational particles, N_p, can always be made equal to the number of real molecules by a proper choice of the computational domain size along the homogeneity directions. In three-dimensional or axisymmetric simulations such a choice is not possible and therefore a weight $\mathscr{W}$ has to be introduced. It should be also observed that, in these cases, the typical DSMC cell size could be smaller than the molecular size and contain less that one *real* molecule. Then, the number of simulation particles could be higher than the real one and the weight can be seen as the inverse of the number of similar real systems that are simulated to obtain good statistics.

As in traditional DSMC implementations, particles positions and velocities are advanced in time by a time splitting scheme, first order accurate in time and in space. During a time step, from time t to time $t+\Delta t$, the distribution function f is first updated by disregarding collisions in Eq. (2). Hence, positions $\mathbf{r}_i$, and velocities $\mathbf{v}_i$, are provisionally given the following values:

$$\mathbf{r}_i(t+\Delta t) = \mathbf{r}_i(t) + \mathbf{v}_i(t)\Delta t + \frac{\mathbf{F}_t[\mathbf{r}_i(t),t]}{m}\frac{(\Delta t)^2}{2}, \tag{18}$$

$$\mathbf{v}_i(t+\Delta t) = \mathbf{v}_i(t) + \frac{\mathbf{F}_t[\mathbf{r}_i(t),t]}{m}\Delta t. \tag{19}$$

The above scheme has first order time accuracy, because of Eq. (19). Once the first step is completed, the variation on f induced by the collision term at the right hand side of Eq. (2) is computed from the equation:

$$\frac{\partial f}{\partial t} = C_{hs}(f,f), \tag{20}$$

which does not describe a locally homogeneous relaxation as it does in the case of Boltzmann equation.

In this second step each particle keeps the position reached at the end of the previous step, whereas particle velocities $\mathbf{v}_i$ are updated according to a probabilistic method which provides an estimate of the overall collision rate in the computational domain and selects collision pairs according to Eq. (20).

We observe that the collision rate of simulation particles is

$$N_c = \frac{1}{2}\sum_{i=1}^{N_p} \nu_i, \tag{21}$$

where

$$\nu_i = \sigma^2 \int \chi_{hs}\left[n\left(\mathbf{r}_i - \frac{\sigma}{2}\hat{\mathbf{k}}\right)\right] f\left(\mathbf{r}_i - \sigma\hat{\mathbf{k}}, \mathbf{v}_1\right)\left[(\mathbf{v}_1 - \mathbf{v}_i)\cdot\hat{\mathbf{k}}\right]^+ d\mathbf{v}_1\, d^2\hat{\mathbf{k}}. \tag{22}$$

To obtain the collision probability of two simulation particles, the computational domain is divided into a number of cells whose size must be small enough to resolve the flow field gradients. Within each cell, the distribution function (17) is spatially regularized and it takes the following form:

$$\tilde{f}(\mathbf{r},\mathbf{v}|t) = \frac{n_m}{N_m}\sum_{j=1}^{N_m}\delta(\mathbf{v}-\mathbf{v}_{mj}), \quad \mathbf{r}\in\mathscr{C}_m. \tag{23}$$

In Eq. (23) n_m and N_m are the real average number density and the number of simulation particles in the $m-th$ cell $\mathscr{C}_m$ respectively, whereas $\mathbf{v}_{mj}$ is the velocity of particle j in $\mathscr{C}_m$. Substituting expression (23) into Eqs. (21) and (22) yields the following result:

$$N_c = \frac{1}{2}\sum_{i=1}^{N_p}\sum_{m=1}^{M_i}\sum_{j=1}^{N_m}\nu_{imj}, \tag{24}$$

$$\nu_{ijm} = \sigma^2\frac{n_m}{N_m}\int_{\mathscr{S}_{im}}\chi_{hs}\left[n\left(\mathbf{r}_i - \frac{\sigma}{2}\hat{\mathbf{k}}\right)\right]\left[(\mathbf{v}_{mj}-\mathbf{v}_i)\circ\hat{\mathbf{k}}\right]^+ d^2\hat{\mathbf{k}}, \tag{25}$$

being M_i the number of cells containing a portion of the sphere having radius a and center $\mathbf{r}_i$, and $\mathscr{S}_{im}$ the region of the unit sphere where $\mathbf{r}_i - \sigma\hat{\mathbf{k}} \in \mathscr{C}_m$. Although correct, the direct evaluation

of N_c from Eq. (24) would require a computational effort proportional to N_p^2. This difficulty is circumvented by the adoption of a majorant collision frequency scheme[41] in which N_c is estimated by a stochastic process. An upper bound $\overline{\nu}_{ijm}$ for each ν_{ijm} is easily obtained as

$$\nu_{ijm} \leq \overline{\nu}_{ijm} = \sigma^2 \frac{A_i C_i}{N_m} \int_{\mathscr{S}_{im}} d^2\hat{\mathbf{k}}, \tag{26}$$

where A_i and C_i satisfy the following inequalities:

$$n_m \chi_{hs} \left[n\left(\mathbf{r}_i - \frac{\sigma}{2}\hat{\mathbf{k}} \right) \right] \leq A_i, \qquad \forall \hat{\mathbf{k}} \in \mathscr{S}_{im}, \quad m = 1 \ldots M_i, \tag{27}$$

$$\mathbf{v}_{mj} - \mathbf{v}_i \leq C_i, \forall mj. \tag{28}$$

An upper bound $\overline{N}_c$ for the collision rate immediately follows from Eq. (26)

$$\overline{N}_c = \frac{1}{2} \sum_{i=1}^{N_p} \sum_{m=1}^{M_i} \sum_{j=1}^{N_m} \overline{\nu}_{imj} = \sum_{i=1}^{N_p} 2\pi\sigma^2 A_i C_i. \tag{29}$$

The method consists in replacing the real collision rate N_c with $\overline{N}_c$ which is easier to obtain. However, the real collision rate will not be altered because the extra collisions will be false collisions which do not change the velocities of colliding pairs.

According to Eq. (29), the probability that particle i is selected for a collision (either real or false) is

$$\overline{p}_i = \frac{2\pi\sigma^2 A_i C_i}{\overline{N}_c}. \tag{30}$$

Once particle i has been selected, the probability it collides with a particle in cell m is

$$\overline{p}_{im} = \frac{\sum_{j=1}^{N_m} \overline{\nu}_{ijm}}{\sum_{m=1}^{M_i} \sum_{j=1}^{N_m} \overline{\nu}_{ijm}} = \frac{1}{4\pi} \int_{\mathscr{S}_{im}} d^2\hat{\mathbf{k}}. \tag{31}$$

Equation (31) shows that $\overline{p}_{im}$ equals the probability that, drawing a random vector $\hat{\mathbf{k}}$ on the unit sphere, the position $\mathbf{r}_i - \sigma\hat{\mathbf{k}}$ of the collision partner is in cell $\mathscr{C}_m$. The probability that particle j out of the N_m particles in $\mathscr{C}_m$ is selected for a collision is

$$\overline{p}_{ijm} = \frac{\overline{\nu}_{ijm}}{\sum_{j=1}^{N_m} \overline{\nu}_{ijm}} = \frac{1}{N_m}. \tag{32}$$

The above result implies that the collision partner of particle i can be chosen at random among the particles in cell $\mathscr{C}_m$. The partner selection rules are based on the modified collision frequencies $\overline{\nu}_{ijm}$ which include false collisions. The probability p_{ijm} that the collision between particles i and

m is real is given by the following expressions:

$$p_{ijm} = \frac{\nu_{ijm}}{\overline{\nu}_{ijm}} = \frac{\int_{\mathscr{S}_{mi}} \phi(\hat{\mathbf{k}})\, d^2\hat{\mathbf{k}}}{\int_{\mathscr{S}_{mi}} d^2\hat{\mathbf{k}}}, \tag{33}$$

$$\phi(\hat{\mathbf{k}}) = \frac{n_m \chi_{hs} \left[n\left(\mathbf{r}_i - \frac{\sigma}{2}\hat{\mathbf{k}}\right)\right] \left[\left(\mathbf{v}_{mj} - \mathbf{v}_i\right) \circ \hat{\mathbf{k}}\right]^+}{A_i C_i}. \tag{34}$$

Since $0 \leq \phi(\hat{\mathbf{k}}) \leq 1$, p_{ijm} is also equal to the probability that a random fraction r_f is less than $\phi(\hat{\mathbf{k}})$, being $\hat{\mathbf{k}}$ uniformly distributed in $\mathscr{S}_{mi}$. If the collision is accepted as real, then the velocities of collision partners are changed according to Eqs. (4) and (5). Since for some applications, the tipical space and time scales of EV based studies of simple fluids are comparable with those typically approached by MD, a comparison of the computational performances of the DSMC scheme described above with those of similar MD simulations is in order.

First of all, it should be noted that the computational effort of each of the two stages composing the DSMC scheme is proportional to the simulation particles number N_p. A similar dependence on N_p holds for MD simulations adopting potential range cut-off and some form of nearest neighbor indexing[40]. For the application described in Section IV, the time step and simulation duration would also be very close. However, the DSMC computational cost per particle is generally smaller. Atoms collisional interaction (stage 2) is treated stochastically, the easily estimated number of collisions to be computed at each time step being much smaller than N_p. The calculation of the self-consistent force field is, in principle, very similar to the way MD computes forces. However, the DSMC computational effort is proportional to the product of the spatial cell number times the number of spatial cells within the cut-off distance. Both factors are much smaller that the number of simulation atoms. Moreover, the numerical calculation of the self-consistent force field can be easily reduced to product of a vector, containing the discretized density field, times a small size matrix whose elements only depend on ϕ_t and can be computed just once and stored to be used throughout the simulation. Nevertheless, it should be also observed that the impact of the force field calculation on the overall DSMC performances depends on the dimensionality of the problem. DSMC-MD comparisons of spatially one-dimensional flow simulations show that DSMC runs about two orders of magnitude times faster than a similar MD simulation with the same atoms number. Comparisons made on two-dimensional flow simulations[36] estimated that DSMC runs about ten times faster than MD, in this case. Such considerations suggest that the computational advantages of DSMC simulations, based on EV equation, are limited to two-dimensional planar and axisymmetric flow geometries. However, it should be kept in mind that Enskog theory

based simulations would be numerically more efficient than MD in the case of weakly non-ideal gases, where the number of real molecules per cubic mean free path would be too high for a deterministic simulation.

IV. EVAPORATION OF A NON-IDEAL VAPOR

The DSMC scheme described above has been applied to study the evaporation of a planar liquid film when the flow conditions produce a non-ideal vapor. The problem is relevant for modeling bubble dynamics[42] and evaporation of fluid droplets[43] but it seems to have received very scant attention, to the authors' knowledge.

The simulation setup has been designed to generate vapor flowfields whose general properties are similar to the classical evaporation of a dilute vapor into a half-space, as described below. In the simplified test problem considered here, a liquid film, in the form of an infinite planar slab of finite thickness Δx_l, is initially in equilibrium with its vapor phase at temperature T_l. The vapor occupies two regions, symmetrically located with respect to the liquid slab center. Each of them is delimited by the adjacent liquid-vapor interface and a perfectly reflecting piston, whose planar surface is kept parallel to the vapor-liquid interface. The left and right pistons are initially located in the vicinity of the vapor-liquid interface at positions $\mp x_p(0)$, respectively. Evaporation flow is started by withdrawing both pistons with constant opposite speeds $\mp V_p$. During evaporation, a narrow strip in the center of the liquid slab is thermostatted at constant temperature T_l to provide the heat flux necessary to sustain evaporation. The resulting flow is unsteady, because of the motion of the interfaces and pistons. However, the common temperature, $T_I(t)$, of the slowly receding interfaces, after an initial rapid transient cooling, reaches a minimum followed by a slow monotonic increase. If the initial slab thickness is large enough, the time evolution of T_I, following the minimum, is so slowly increasing to be considered a constant plateau. In this phase of the system evolution, the temperature profile in the liquid takes an approximately linear shape evolving self-similarly. If the duration of the temperature plateau is long enough with respect to the time sound waves in the vapor take to travel through the gap between the piston and the interface, then the vapor flow becomes quasi-steady. Its structure is relatively simple, consisting of a kinetic region (Knudsen layer) next to the interface, followed by a uniform equilibrium region where the vapor moves with the piston speed, the density and temperature profiles being nearly constant.

DSMC simulations, following the scheme depicted above, have been performed starting from the

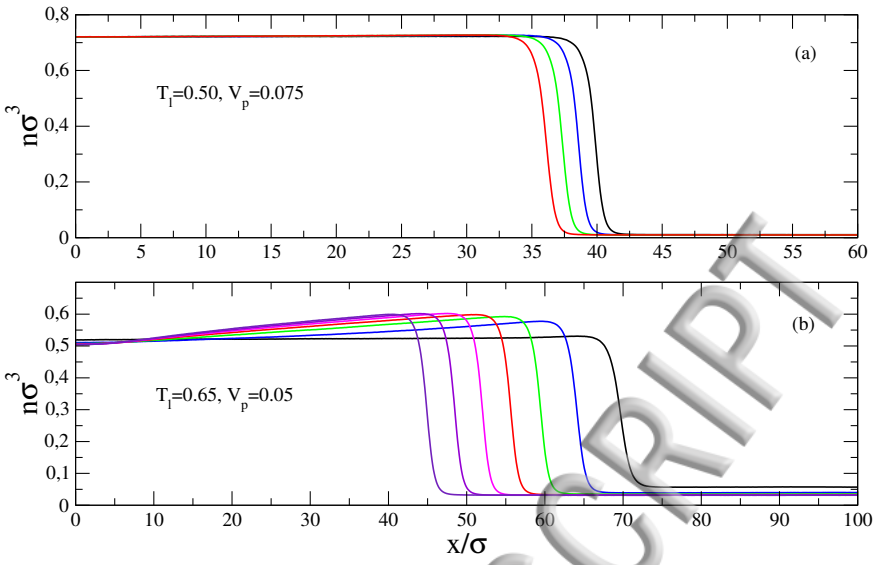

FIG. 2. Time evolution of fluid density during evaporation of a liquid film. **(a)** $T_l = 0.50$, $V_p = 0.075$: $t = 100$ (black), $t = 1300$ (blue), $t = 2500$ (green), $t = 3700$ (red). **(b)** $T_l = 0.650$, $V_p = 0.05$: $t = 100$ (black), $t = 1300$ (blue), $t = 2500$ (green), $t = 3700$ (red), $t = 4900$ (magenta), $t = 6100$ (violet), $t = 7300$ (indigo).

vapor-liquid equilibrium solutions listed in Table I. For each temperature value, three simulations with piston velocities $V_p = (5.0e-02, 7.5e-02, 1.0e-01)$, in units of $\sqrt{\phi_\sigma/m}$. In the following, reduced units are used: the hard sphere diameter σ is the reference length, the molecular mass m is the reference mass and $\sigma\sqrt{m/\phi_\sigma}$ the reference time. Accordingly, the number density, velocities and temperatures are given, respectively, in units of σ^{-3}, $\sqrt{\phi_\sigma/m}$ and ϕ_σ/k_B, being k_B the Boltzmann constant.

It is worth mentioning that breaking of the liquid slab prevented from obtaining useful results at the highest temperature value, $T = 0.7$, corresponding to about 93% of the critical temperature. Because of the intrinsic flow unsteadiness, macroscopic flowfields have been obtained by a combination of phase and time averaging, in order to improve the quality of statistics in the less populated vapor phase. For each temperature and piston velocity combination, 12 statistically independent but macroscopically equivalent simulations have been run. Each simulation used 10^6 particles, a grid size of $1/10$ and a time step of 5.0e-03. Within each simulation, time averaging has been performed over a time window which is long with respect to molecular scale but relatively short with respect to the vapor phase time scale. Moreover, the amplitude of the time averaging window has been kept short enough to have neglible interfaces displacement during the averaging process.

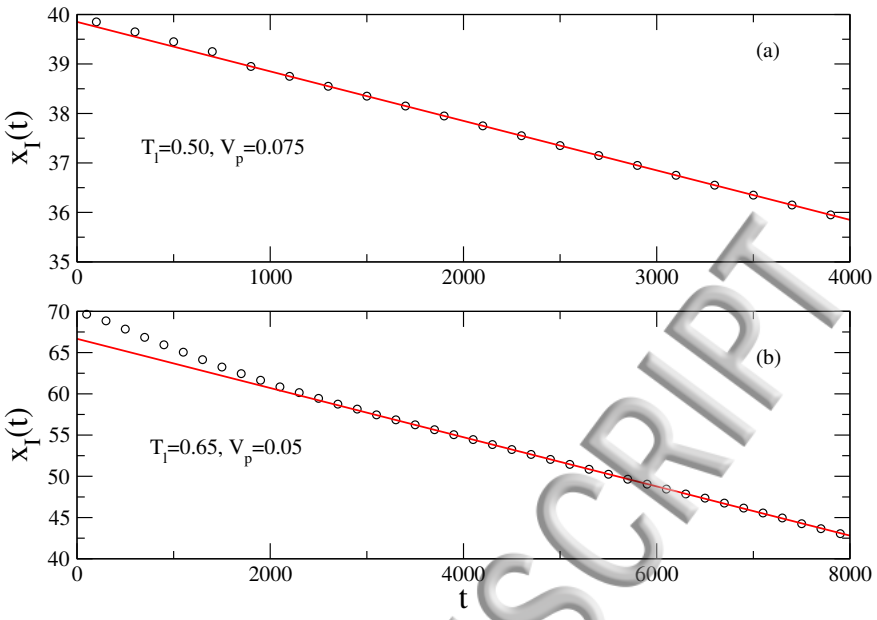

FIG. 3. Time histories of interface position during evaporation of a liquid film. **(a)** $T_l = 0.50$, $V_p = 0.075$. ○: DSMC simulation data; red solid line: linear regression in time window $1000 < t < 4000$. **(b)** $T_l = 0.650$, $V_p = 0.05$. ○: DSMC simulation data; red solid line: linear regression in time window $4000 < t < 8000$.

Thanks to the relatively high simulation particle number, statistical run to run variations are small. In particular, the relative error associated with global flow properties (like T_∞ and n_∞, for instance) is well below 1.0%. Figure 2 shows the time evolution of the fluid density profile for two cases corresponding to the lowest and highest values of T_l considered here. For $T_l = 0.5$, the vapor is close to ideal conditions (see Table I); the small value of the piston velocity, $V_p = 0.075$, produces a small evaporation mass flux and a small evaporative cooling of the interface. As a result, the density profile simply recedes while approximately keeping its equilibrium shape. For $T_l = 0.65$, the vapor density is much higher. Hence, evaporation causes stronger cooling of the interface leading to a more pronounced transient, during which the liquid density in the interface region increases whereas the vapor density decreases, with respect to the equilibrium value. The initial rapid surface cooling is followed by a flow regime in which the interfacial density profile keeps the same shape, receding with fairly constant velocity, as shown by the four leftmost curves in Fig. 2. In order to give a more quantitative description, the interface motion has been followed by defining its position $x_I(t)$ as the point where the absolute value of the spatial derivative of the density profile $|\frac{\partial n}{\partial x}(x,t)|$ has a maximum. The time histories of the interface position, corresponding to the cases considered in Fig. 2, are shown in Fig. 3. In the low temperature case, the initial transient

can be hardly detected and the interface appears to move with constant velocity over most of the simulation time.

The transient cooling effect is more evident in the second case, where the temperature is higher and initially causes more intense evaporation and faster interface recession, before the onset of the (approximately) constant velocity recession.

The comparison with the dilute gas approximation, provided by the Boltzmann equation and the companion boundary conditions, requires that a temperature is attributed to the vapor liquid interface. This is a delicate point which has been addressed in different ways[33,44,45]. Figure 4 shows the flowfield structures in the vicinity of the interfaces in two flow conditions having identical piston speeds, $V_p = 0.10$, but different temperatures and initial liquid slab thickness, respectively set equal to: $T_l = 0.50$, $\Delta x_l = 80.0$ (left panel) and $T_l = 0.65$, $\Delta x_l = 140.0$ (right panel). Both flowfields belong to the quasi-steady regime described above. The position of the interface is given by the maximum of the absolute value of the density gradient, marked by the vertical dashed lines. The intensity of the maximum also shows that the interface thickness increases with temperature[21]. The above definition of the interface position is more than simply conventional. Actually, this is also the point where the velocity starts accelerating towards V_p and where the longitudinal, transversal and overall temperatures, $T_\parallel(x)$, $T_\perp(x)$ and $T(x) = (T_\parallel(x) + 2T_\perp(x))/3$, separate. The temperatures mentioned above are defined as:

$$T_\parallel(x) = \frac{1}{n(x)R} \int [v_x - u_x(x)]^2 f(x, \mathbf{v})\, d^3v\,, \tag{35}$$

$$T_\perp(x) = \frac{1}{2n(x)R} \int (v_y^2 + v_z^2) f(x, \mathbf{v})\, d^3v\,, \tag{36}$$

$$T(x) = \frac{T_\parallel(x) + 2T_\perp(x)}{3}\,, \tag{37}$$

and their separation marks the beginning of the kinetic region where the distribution function becomes anisotropic because of the mixing of two different molecular groups. The first one, moving with velocities $v_x > 0$, is formed by the molecules spontaneously evaporating from the interface. The second one, moving with velocities $v_x < 0$, is formed by the molecules which have already suffered a number of collisions in the gas phase and are being scattered back to the interface. The distribution function of the first group is well represented by a half-range ($v_x > 0$) Maxwellian (see Refs. 33 and 46 for a more detailed discussion), characterized by a temperature extremely close to the fluid temperature at the separation position. The second group is well represented by a drifting Maxwellian with a lower temperature, produced by the vapor expansion.

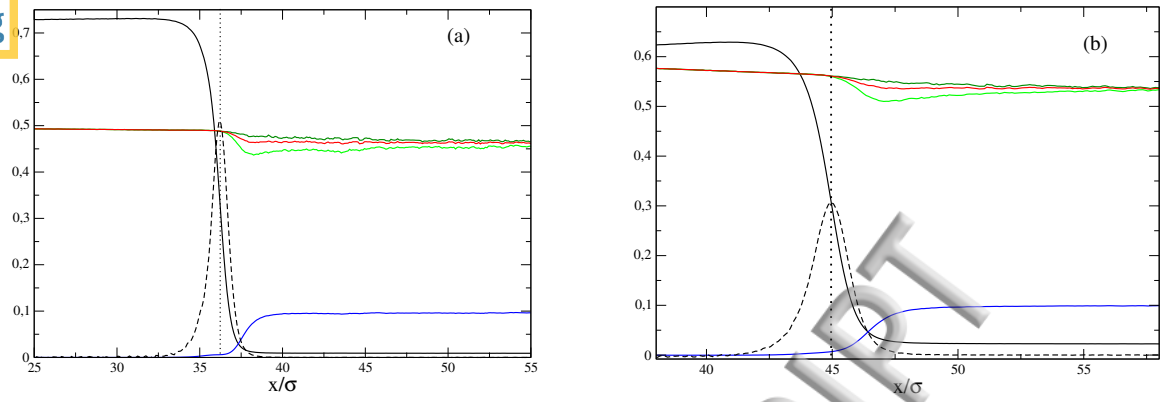

FIG. 4. Density, velocity and temperature profiles in the *quasi-steady* regime. **(a)**- $T_l = 0.50$, $V_p = 0.10$: density $n(x)$ (black solid line), density gradient $\left|\frac{\partial n}{\partial x}\right|$ (black dashed line), velocity u_x (blue solid line), longitudinal temperature $T_{\parallel}(x)$ (light green solid line), transversal temperature $T_{\perp}(x)$ (green solid line), temperature $T(x) = (T_{\parallel}(x) + 2T_{\perp}(x))/3$ (red solid line). The vertical dashed line marks the position of the density gradient maximum. **(b)**- $T_l = 0.65$, $V_p = 0.10$: line marking same as on left panel.

In this work, the vapor-liquid interface temperature, $T_I(t)$, has been defined as $T(x_I, t)$, *i.e.* as the fluid temperature at the interface position. As noted above, x_I seems to mark the onset of temperatures separations. Such statement is only approximately correct. However, a closer examination of the simulation data shows that setting the temperature separation position, x_{sep}, as the point where $(T_{\perp} - T_{\parallel})/T$ exceeds a given threshold (say 0.1%) puts x_{sep} within only 0.1σ from x_I and the corresponding separation temperature differs from T_I less than 0.5% in all considered cases. It is also worth stressing that, in absence of a more rigorous definition, assigning to the interface the temperature T_I, defined above, should be considered a reasonable working assumption. However, it should also be noted that such definition has been found to be consistent with the continuum-kinetic description of the evaporation of the Lennard-Jones fluid presented in Ref. 47. There, the evaporation of a liquid slab, *in the dilute vapor regime*, has been studied by MD simulations of the Lennard-Jones fluid and by a hybrid model, combining a continuum description of the liquid phase with a kinetic description of the vapor. The liquid and vapor regions have been connected by the kinetic boundary condition described below by Eqs. (40), (41) and (42), which replace the real liquid-vapor interface. Particular care has been taken to tune the thermodinamic and transport properties of the continuum model to those of the Lennard-Jones fluid. The hybrid model has successfully reproduced MD results. In particular, the time evolution of the liquid surface temperature predicted by the hybrid model has very well matched the $T_I(t)$ time hystory obtained

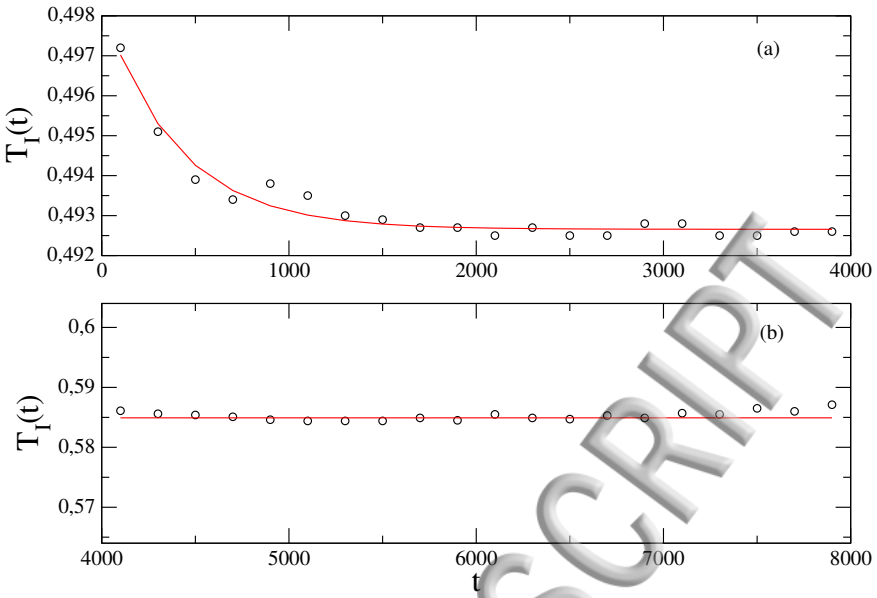

FIG. 5. Time histories of interface temperature T_I during evaporation of a liquid film. **(a)** $T_l = 0.50$, $V_p = 0.075$. ○: DSMC simulation data; red solid line: exponential regression in time window $100 < t < 4000$. **(b)** $T_l = 0.650$, $V_p = 0.05$, closeup of the T_I plateau time region ○: DSMC simulation data; the red horizontal line represents the T_I average in a time window centered around $t = 6000$ and about 2500 time units wide.

from MD simulations, following the same definition given above. Very good agreement has also been obtained for the evaporation rate and Knudsen layer structure in the vapor phase. Figure 5 presents examples of the time history of the interface temperature T_I for the same flow conditions for which Fig. 3 displays the corresponding interface positions. As shown by the upper panel, T_I exhibits an exponential decay towards a temperature plateau, the decay rate being determined by the initial slab thickness and by the evaporation rate. The lower panel presents a closeup of the interface temperature in the interval $4000 < t < 8000$ which includes the tail of the exponential decay on the left and the beginning of the temperature increase on the right. The latter is caused by the steepening of the temperature profile in the liquid phase whose thickness is reducing, thus increasing the amount of heat conducted towards the interface, from the thermostatted central region. However, in a time window around the center of the interval, about 2500 time units wide, the small temperature variation is comparable with the statistical noise and the interface temperature is assigned its time averaged value as far as the following comparison with classical kinetic theory is concerned.

In the quasi-steady flow regime, evaporation produces fairly uniform and constant equilibrium

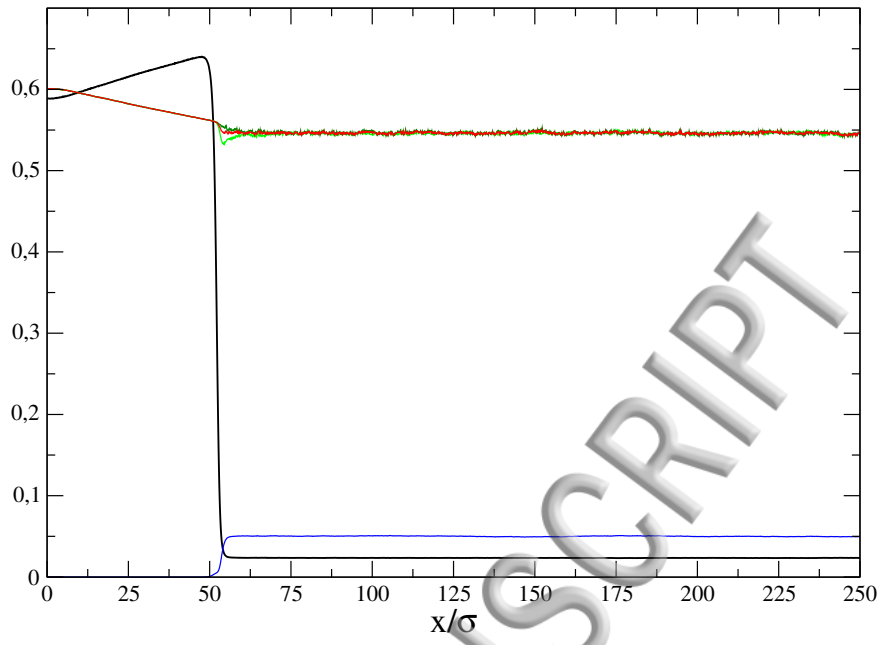

FIG. 6. Flowfield structure for $T_l = 0.60$, $V_p = 0.05$ and $\Delta x_l = 140$. Density $n(x)$ (black solid line), velocity u_x (blue solid line), longitudinal temperature $T_{\parallel}(x)$ (light green solid line), transversal temperature $T_{\perp}(x)$ (green solid line), temperature $T(x) = (T_{\parallel}(x) + 2T_{\perp}(x))/3$ (red solid line).

flowfield outside the kinetic region, characterized by the density n_∞, temperature T_∞ and bulk velocity $u_\infty = V_p$.

Figure 6 shows an example of the computed flowfield, where most of the computational domain is occupied by the equilibrium vapor region. In general, the asymptotic values of density and temperature, n_∞ and T_∞, have been obtained from simulation data by spatial averaging over a region, a few hundred molecular diameters wide, which excludes the kinetic regions next to the interface and the piston surface. Table II gathers the results of the simulations and presents for each flow setting, the average interface temperature T_I and the saturated number density, $n_{sat}(T_I)$, and pressure, $p_{sat}(T_I)$, obtained from the coexistence curve. It is possible to note that, at high temperature T_l, even small downstream flow velocity can cause strong surface cooling and consequent vapor thinning. Hence, any deviation from ideality during evaporation is likely to be confined to weak evaporation conditions. The downstream flow properties obtained from the simulations are given in Table III, as a function of flow setting. Columns $3-6$ contain the downstream values of vapor temperature, density and pressure which provide the jumps macrosopic vapor properties suffer across the kinetic layer. The deviation from the ideal behavior is given by the mean free path $\lambda_\infty = 1/[\sqrt{2}\pi n \chi_{hs}(n_\infty)]$, based on hard sphere interaction and the vapor compressibility

T_l	V_p	Δx_l	T_I	$n_{sat}(T_I)$	$p_{sat}(T_I)$
5.00e-01	5.00e-02	8.00e+01	4.98e-01	1.20e-02	5.51e-03
5.00e-01	7.50e-02	8.00e+01	4.93e-01	1.11e-02	5.08e-03
5.00e-01	1.00e-01	8.00e+01	4.88e-01	1.04e-02	4.76e-03
5.50e-01	5.00e-02	8.00e+01	5.36e-01	1.95e-02	9.27e-03
5.50e-01	7.50e-02	8.00e+01	5.28e-01	1.77e-02	8.38e-03
5.50e-01	1.00e-01	8.00e+01	5.22e-01	1.65e-02	7.77e-03
6.00e-01	5.00e-02	1.40e+02	5.59e-01	2.57e-02	1.24e-02
6.00e-01	7.50e-02	1.40e+02	5.47e-01	2.24e-02	1.07e-02
6.00e-01	1.00e-01	1.40e+02	5.39e-01	2.03e-02	9.69e-03
6.50e-01	5.00e-02	1.40e+02	5.85e-01	3.43e-02	1.67e-02
6.50e-01	7.50e-02	1.40e+02	5.71e-01	2.94e-02	1.42e-02
6.50e-01	1.00e-01	2.00e+02	5.49e-01	2.29e-02	1.10e-02

TABLE II. Interface temperature T_I and saturated vapor density and pressure, $n_{sat}(T_I)$, $p_{sat}(T_I)$, as a function flow parameters T_l, V_p, and Δx_l.

$Z_\infty = p(n_\infty, T_\infty)/(n_\infty T_\infty)$. Reported data show that, as expected, increasing V_p brings the downstream vapor condition closer to ideality, whereas increasing T_l produces denser vapor and, if V_p is kept small enough, downstream conditions are rather far from ideal, being λ_∞ below 10 molecular diameters.

The quantity $H_\infty = [p_\infty - p_{sat}(T_\infty)]/p_{sat}(T_\infty)$ which measures the relative deviation of the actual vapor pressure from its saturation value at T_∞, indicates that the vapor expansion across the Knudsen layer tends to produce supersaturation. The last two columns report, respectively, the downstream flow Mach number $M_\infty = V_p/c_\infty$ and its ideal limit value $M_\infty^{(id)} = \sqrt{3/(5T_\infty)}V_p$, the former being based on the non-ideal sound speed value, obtained as:

$$c^2(n,T) = \frac{\partial p}{\partial n} + \frac{\partial p}{\partial T}\left(\frac{\partial e}{\partial T}\right)^{-1}\left(\frac{p}{n^2} - \frac{\partial e}{\partial n}\right), \tag{38}$$

being $e(n,T) = \frac{3T}{2} - \frac{2\pi}{3}n$ the fluid specific energy, in reduced units.

T_l	V_p	Δx_l	T_∞	n_∞	p_∞	λ_∞	Z_∞	H_∞	M_∞	$M_\infty^{(id)}$
5.00e-01	5.00e-02	8.00e+01	4.86e-01	1.10e-02	4.94e-03	2.03e+01	9.29e-01	8.59e-02	5.81e-02	5.56e-02
5.00e-01	7.50e-02	8.00e+01	4.75e-01	9.75e-03	4.33e-03	2.28e+01	9.34e-01	1.32e-01	8.78e-02	8.43e-02
5.00e-01	1.00e-01	8.00e+01	4.63e-01	8.81e-03	3.83e-03	2.53e+01	9.39e-01	2.31e-01	1.18e-01	1.14e-01
5.50e-01	5.00e-02	8.00e+01	5.21e-01	1.77e-02	8.28e-03	1.24e+01	8.96e-01	7.18e-02	5.70e-02	5.40e-02
5.50e-01	7.50e-02	8.00e+01	5.08e-01	1.55e-02	7.14e-03	1.42e+01	9.05e-01	1.17e-01	8.65e-02	8.15e-02
5.50e-01	1.00e-01	8.00e+01	4.94e-01	1.39e-02	6.26e-03	1.59e+01	9.12e-01	2.08e-01	1.17e-01	1.10e-01
6.00e-01	5.00e-02	1.40e+02	5.46e-01	2.34e-02	1.11e-02	9.32e+00	8.71e-01	4.75e-02	5.69e-02	5.24e-02
6.00e-01	7.50e-02	1.40e+02	5.29e-01	1.97e-02	9.23e-03	1.11e+01	8.86e-01	8.65e-02	8.59e-02	7.99e-02
6.00e-01	1.00e-01	1.40e+02	5.17e-01	1.72e-02	7.98e-03	1.28e+01	8.97e-01	1.03e-01	1.15e-01	1.08e-01
6.50e-01	5.00e-02	1.40e+02	5.75e-01	3.18e-02	1.53e-02	6.79e+00	8.38e-01	2.48e-02	5.66e-02	5.11e-02
6.50e-01	7.50e-02	1.40e+02	5.51e-01	2.61e-02	1.23e-02	8.34e+00	8.58e-01	9.07e-02	8.56e-02	7.83e-02
6.50e-01	1.00e-01	2.00e+02	5.25e-01	1.95e-02	9.05e-03	1.13e+01	8.87e-01	1.13e-01	1.15e-01	1.07e-01

TABLE III. Downstream equilibrium flow properties as a function of flow parameters T_l, V_p, and Δx_l.

A. Comparisons with ideal gas theory

When the saturated vapor pressure is low enough, the vapor behaves as an ideal gas. Then, the vapor flow, relative to the moving interface, is well decribed by the classical half-space solutions[30,48] of the steady Boltzmann equation for a dilute hard sphere gas[2]:

$$v_x \frac{\partial f}{\partial x} = \frac{\sigma^2}{2} \int_{\mathscr{S}} \{ f(\mathbf{r}, \mathbf{v}_1^*, t) f(\mathbf{r}, \mathbf{v}^*, t) - f(\mathbf{r}, \mathbf{v}_1, t) f(\mathbf{r}, \mathbf{v}, t) \} \, |\mathbf{v}_r \cdot \hat{\mathbf{k}})| d\mathbf{v}_1 d^2\hat{\mathbf{k}}. \tag{39}$$

At the spatial location of the assumed planar and structureless interface, the following boundary condition holds:

$$v_x f(\mathbf{v}, t) = v_x f_e(\mathbf{v}) + \int_{v_x'<0} K(\mathbf{v}, \mathbf{v}') |v_x'| f(\mathbf{v}', t) \, d^3\mathbf{v}', \quad v_x > 0, \tag{40}$$

which mimics the presence of the vapor-liquid interface that Eq. (39) cannot describe. Equation (40) assigns the molecular flux emerging from the interface as the superposition of two distinct components. The first one consists of the molecules initially belonging to the liquid phase and evaporating into the vapor phase with distribution function $f_e(\mathbf{v})$, the second one consists of vapor molecules whose initial velocity $\mathbf{v}'$ is instantaneously changed to $\mathbf{v}$ as a results of the vapor-liquid surface scattering, described by the kernel $K(\mathbf{v}, \mathbf{v}')$[2]. The usual choice for the distribution

function $f_e(\mathbf{v})$ of molecules evaporating from the condensed phase is the half range Maxwellian

$$f_e(\mathbf{v}) = \sigma_e \frac{n_{sat}(T_I)}{(2\pi R T_I)^{3/2}} \exp\left(-\frac{\mathbf{v}^2}{2RT_I}\right), \quad v_x > 0, \tag{41}$$

whereas Maxwell's gas-surface scattering kernel is the usual choice to describe scattering of vapor molecules impinging on the liquid surface:

$$K(\mathbf{v},\mathbf{v}') = (1-\sigma_e)\left[\alpha v_x \frac{1}{2\pi(RT_I)^2} \exp\left(-\frac{\mathbf{v}^2}{2RT_I}\right) + (1-\alpha)\delta(\mathbf{v}-\mathbf{v}'+2v'_x\hat{\mathbf{x}})\right]. \tag{42}$$

In the above expressions, $n_{sat}(T_I)$ is the number density of the saturated vapor at the temperature of the interface T_I. The evaporation/condensation coefficient σ_e ($0 \leq \sigma_e \leq 1$) gives the fraction of vapor molecules impinging on the interface and absorbed. The total fraction of impinging molecules which are *instantaneously* re-emitted is $1-\sigma_e$, α being the probability of diffuse re-emission and $1-\alpha$ the probability of specular reflection from a surface whose normal is $\hat{\mathbf{x}}$.

It is further assumed that, far from the vapor-liquid interface, the vapor distribution function is a Maxwellian. More precisely:

$$\lim_{x\to\infty} f(x,\mathbf{v}) = \frac{n_\infty}{(2\pi R T_\infty)^{\frac{3}{2}}} \exp\left[-\frac{(\mathbf{v}-u_\infty\hat{\mathbf{x}})^2}{2RT_\infty}\right], \tag{43}$$

being n_∞, u_∞ and T_∞ the downstream values of vapor number density, velocity, and temperature, respectively.

The flow properties in the dilute gas limit have obtained by many studies of steady evaporation into a half-space, based on kinetic equations[48] or moment equations[49]. The main results can be summarized by the following statements:

1. In the flow settings specified above, steady flows are possible only when the downstream equilibrium state is sub-sonic.

2. The downstream equilibrium density n_∞ and temperature T_∞ are related to the liquid interface temperature T_I and saturated vapor density $n_{sat}(T_I)$ by the following formal relationships:

$$\frac{T_\infty}{T_I} = \frac{T_\infty}{T_I}(M_\infty), \tag{44}$$

$$\frac{n_\infty}{n_{sat}(T_I)} = \frac{n_\infty}{n_{sat}(T_I)}(M_\infty), \tag{45}$$

where M_∞ the downstream flow Mach number. The form of the two above relationships implies that both the density and temperature jumps across the Knudsen layer are determined by a single parameter, M_∞. The determination of precise form of Eqs. (44) and (45) is not any easy task since it requires the solution of the Boltzmann equation or a kinetic model equation. Analytical results are available for weak evaporation, described by the linearized Boltzmann equation[50]. Analytical results for arbitrary subsonic values of M_∞ have been obtained by T. Ytrehus[46] for Maxwellian molecules[2] by the method of moments. Numerical results for arbitrarily strong subsonic evaporation for a monatomic gas described by the BGKW model and by the full hard sphere Boltzmann equation, solved by DSMC, are respectively presented in Refs. 51 and 52.

The form of Eqs. (44) and (45) also depends on the parameters appearing in the vapor-liquid boundary condition model, although most of the studies have assumed either unit evaporation coefficient or arbitrary $\sigma_e < 1$, but purely diffuse scattering of the reflected molecules ($\alpha = 1$ in Eq. (40)). Since Eqs. (44) and (45) (partially) provide the link between the hydrodynamic descriptions of the liquid and vapor phases through the kinetic layer, it is of interest to assess the validity of the above ideal kinetic description of evaporation from a liquid surface when the vapor is no longer dilute.

In principle, it is to be expected that deviations from the dilute limit behavior might appear when the mean free path in the vapor phase becomes comparable with the molecular size. Moreover, the usual form of kinetic boundary conditions at the vapor-liquid interface, might become not adequate in a situation in which the time a gas phase molecules spends interacting with the liquid phase is comparable with vapor phase collision time. The comparison with the results obtained from the dilute gas limit has been based on a series of accurate DSMC simulations for a hard sphere gas, governed by the Boltzmann equation. The vapor-liquid interface boundary condition as given by Eqs. (40-42) has been used. In particular, T_I and $n_{sat}(T_I)$ have been assigned the values obtained by the companion EV simulation (see Table II). The evaporation coefficient has been set equal to one, although lower values have been also considered in a few exploratory simulations. The boundary condition at infinity, Eq. (43), has been dealt with by the method described in Refs. 52 and 53. The asymptotic vapor velocity u_∞ has been set equal to $V_p - V_I$, being V_I the interface recession velocity, obtained by the EV simulation. Actually, Eq. (39) is meant to describe the steady vapor flow observed by the reference frame moving with the uniformly receding interface. In principle, the liquid bulk behind the still interface would have a velocity $-V_I$ in the co-moving frame. Accordingly, the same velocity should also be added to f_e, in Eq. (40). However, the simulation results in

$T_\infty^{(ev)}$	$T_\infty^{(be)}$	ε_T	$n_\infty^{(ev)}$	$n_\infty^{(be)}$	ε_n
4.86e-01	4.86e-01	-8.23e-04	1.09e-02	1.10e-02	-4.36e-03
4.75e-01	4.75e-01	2.11e-04	9.75e-03	9.77e-03	-2.08e-03
4.63e-01	4.66e-01	-6.33e-03	8.81e-03	8.81e-03	0.00e+00
5.21e-01	5.24e-01	-3.97e-03	1.77e-02	1.79e-02	-9.49e-03
5.08e-01	5.10e-01	-3.31e-03	1.55e-02	1.56e-02	-6.13e-03
4.94e-01	4.97e-01	-7.98e-03	1.39e-02	1.40e-02	-4.80e-03
5.46e-01	5.46e-01	5.68e-04	2.34e-02	2.36e-02	-8.63e-03
5.29e-01	5.28e-01	4.92e-04	1.97e-02	1.98e-02	-4.14e-03
5.17e-01	5.14e-01	4.78e-03	1.72e-02	1.72e-02	2.91e-04
5.75e-01	5.72e-01	5.95e-03	3.18e-02	3.16e-02	3.89e-03
5.51e-01	5.51e-01	-5.62e-04	2.61e-02	2.60e-02	4.54e-03
5.25e-01	5.24e-01	1.13e-03	1.94e-02	1.95e-02	-7.71e-04

TABLE IV. Downstream density $n_\infty^{(ev)}$ and temperature $T_\infty^{(ev)}$ obtained from EV simulations compared with corresponding values, $n_\infty^{(be)}$ and $T_\infty^{(be)}$, obtained from Boltzmann equation DSMC simulations. Relative deviations are defined as $\varepsilon_T = (T_\infty^{(ev)} - T_\infty^{(be)})/(T_\infty^{(be)})$, $\varepsilon_n = (n_\infty^{(ev)} - n_\infty^{(be)})/(n_\infty^{(be)})$. Data ordering is the same as in Tables II and III.

which the liquid drift velocity has been taken into account are practically indistinguishable from those obtained keeping f_e as in Eq. (41). DSMC simulations have been run using not less than 1500 particles per cell and a grid size of $\lambda_I/20$, being λ_I the reference mean free path in the vapor, in equilibrium at temperature T_I with density $n_{sat}(T_I)$.

Simulation results, based on EV and Boltzmann equations, are compared in Table IV, which shows that temperature and density jumps predicted by the two kinetic equations are extremely close, even in the cases where the deviation from ideality is not small and the ratio of nominal mean free path to the molecular size is well below 10. The same results are given in visual form in Fig. 7 which gives EV and Boltzmann computed jumps as a function of the dowstream speed ratio $S_\infty = u_\infty/\sqrt{2T_I}$ and compares DSMC data with the linearized jump formulas reported in Ref. 54 for a dilute monatomic gas, described by a kinetic model.

$$\frac{n_\infty - n_{sat}(T_I)}{n_{sat}(T_I)} = -1.6853\,S_\infty, \qquad \frac{T_\infty - T_I}{T_I} = -0.4468\,S_\infty. \tag{46}$$

Again, the results show that EV results are very close to those derived by ideal gas theory and

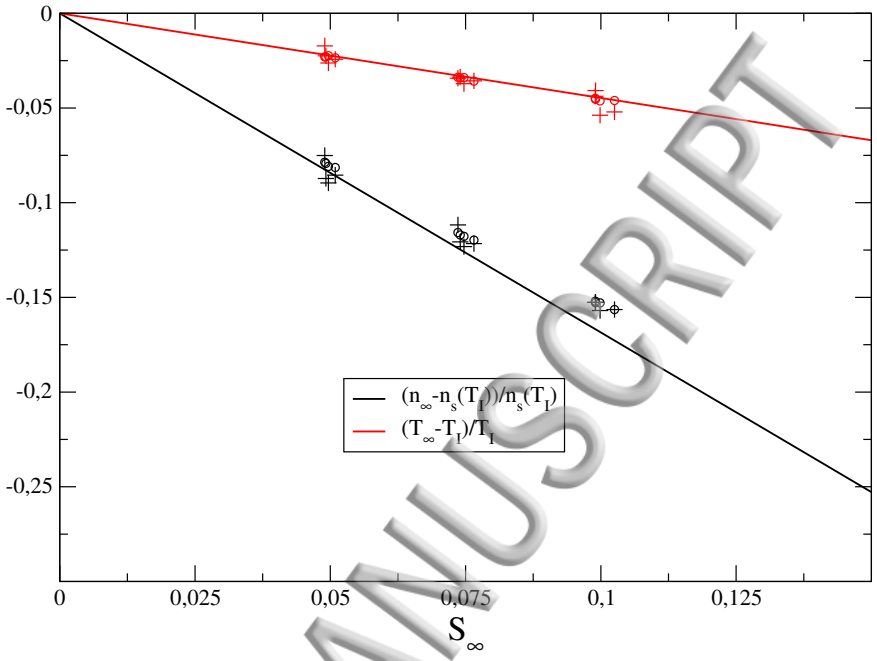

FIG. 7. Density and temperature jumps as a function of speed ratio S_∞. Black solid line: density jump from *dilute gas linearized theory*[54]; black ○: density jump from Boltzmann equation DSMC simulations; black +: density jump from EV equation DSMC simulations. Red solid line: temperature jump from *dilute gas linearized theory*[54]; red ○: temperature jump from Boltzmann equation DSMC simulations; red +: temperature jump from EV equation DSMC simulations.

that, for weak evaporation, existing linearized jump formulas would give a close approximation of density and temperature jumps in a non-ideal fluid described by the EV equation. Before concluding, a few observations are in order. The deviation of the density jump from the linearized formula, exhibited by both EV and Boltzmann equations data, is due to non-linear effects which show up on the density drop but not yet on the temperature drop, at low values of S_∞. Non-ideality does not manifest if jumps are expressed as a function of S_∞ but it would modify jump formulas using M_∞ in place of S_∞ because of the difference between M_∞ and $M_\infty^{(id)}$ mentioned above. The same observation applies to the pressure jump formula which could be obtained by Eqs. (46), by taking into account the compressibility Z to correct the ideal pressure jump formula.

V. CONCLUSIONS

As stated in the Introduction, the paper aims at showing that DSMC structure is general and robust enough to allow extensions towards non-ideal fluids, governed by Enskog-like equations. It should be stressed once again that within the framework of the theory and applications of kinetic theory of dense fluids, the role of DSMC is even stronger than in its ideal gas counterpart, because of the considerably more complicated mathematical structure of underlying equations. Particular attention has been given to reviewing applications of DSMC to vapor-liquid flows described by the Enskog-Vlasov equation, where the numerical method, so far the only way to approach its non-equilibrium solutions, is contributing to a better understanding of transport processes across the liquid-vapor interface. As example of application, the evaporation of non-ideal vapor in contact with its condensed phase has been described and discussed. More specifically, the question has been addressed on the validity of the jump relationships of the macroscopic quantities across the Knudsen layer. Indeed, studies carried out until now were based on the assumption that the gas is ideal and it was not clear whether or not results are affected by a compressibility factor in the vapor phase significantly different from unity. Simulation results suggest that the usual jumps relationships also apply to non-ideal vapors as long as the independent parameter in these formula is the downstream speed ratio. However, this conclusion has to be considered as preliminary and more work is needed to enlarge the simulations data base and confirm that the result is not a consequence of the simplified treatment of dense fluids provided by the EV equation. It is also worth mentioning that the use of EV model is not limited to the application described above. Once provided with a suitable fluid-solid interaction model[36], it can be applied to investigate confined flows. In particular, two-phase flows in porous media[55] and the dynamics of droplet impacts, leading to evaporation phenomena[56], appear to be promising fields of application.

VI. ACKNOWLEDGEMENT

It is a honor to have the opportunity to dedicate this paper to the memory of Professor G. A. Bird. Although these few lines are not enough to do justice to his work and the huge impact it had on the community of kinetic theory of fluids, one of authors (AF) would like to express gratitude for the encouragement received by G. A. Bird during the development of the techniques described here.

REFERENCES

[1]G. A. Bird. Approach to translational equilibrium in a rigid sphere gas. *Phys. Fluids*, 6(10):1518–1519, 1963.

[2]C. Cercignani. *The Boltzmann Equation and Its Applications*. Springer-Verlag, Berlin, 1988.

[3]G. A. Bird. Direct simulation and the Boltzmann equation. *Phys. Fluids*, 13(11):2676–2681, 1970.

[4]G. A. Bird. *Molecular Gas Dynamics and the Direct Simulation of Gas Flows*. Clarendon Press, Oxford, 1994.

[5]P. Resibois and M. DeLeener. *Classical Kinetic Theory of Fluids*. J. Wiley & Sons, New York, 1977.

[6]F. J. Alexander, A. L. Garcia, and B. J. Alder. The consistent Boltzmann algorithm for the Van der Waals equation of state. *Physica A*, 240:196–201, 1997.

[7]A. L. Garcia, F. J. Alexander, and B. J. Alder. A particle method with adjustable transport properties - the generalized consistent Boltzmann algorithm. *J. Stat. Phys.*, 89:403–409, 1997.

[8]A. L. Garcia and W. Wagner. The limiting kinetic equation of the consistent Boltzmann algorithm for dense gases. *J. Stat. Phys.*, 101:1065–1086, 2000.

[9]D. Enskog. Kinetische theorie der wärmeleitung, reibung und selbstdiffusion in gewissen verdichteten gasen und flüssigkeiten. *Kungl. Svenska Vet.-Ak. Handl.*, 63, 1922.

[10]H.J.M. Hanley, R.D. McCarty, and E.G.D. Cohen. Analysis of the transport coefficients for simple dense fluid: Application of the modified Enskog theory. *Physica*, 60(2):322–356, 1972.

[11]A. Frezzotti. Molecular dynamics and Enskog theory calculation of one dimensional problems in the dynamics of dense gases. *Physica A*, 240(1):202–211, 1997.

[12]J. M. Montanero and A. Santos. Monte Carlo simulation method for the Enskog equation. *Phys. Rev. E*, 54(1):438–444, 1996.

[13]K. Nambu. Theoretical basis of the Direct Simulation Monte Carlo method. In C. Cercignani and V. Boffi, editors, *Proceedings of the 15th International Symposium on Rarefied Gas Dynamics*, volume 1, pages 369–383, Stuttgart, 1986. Teubner Verlag.

[14]C. Greengard and L. G. Reyna. Conservation of expected momentum and energy in Monte Carlo particle simulation. *Phys. Fluids A*, 4(4):849–852, 1992.

[15]A. Frezzotti. A particle scheme for the numerical solution of the Enskog equation. *Phys. Fluids*, 9(5):1329–1335, 1997.

[16]J. M. Montanero and A. Santos. Simulation of the Enskog equation à la Bird. *Phys. Fluids*, 9(7):2057–2060, 1997.

[17]N. V. Brilliantov and T. Pöschel. *Kinetic Theory of Granular Gases*. Oxford University Press, 2010.

[18]A. Frezzotti. DSMC simulation of the vertical structure of planetary rings. *Astron. Astrophysics*, 380:761–775, 2001.

[19]L. de Sobrino. On the kinetic theory of a Van der Waals gas. *Can. J. Phys.*, 45(2):363–385, 1967.

[20]M. Grmela. Kinetic equation approach to phase transitions. *J. Stat. Phys.*, 3:347–364, 1971.

[21]A. Frezzotti, L. Gibelli, and S. Lorenzani. Mean field kinetic theory description of evaporation of a fluid into vacuum. *Phys. Fluids*, 17(1):012102, 2005.

[22]J. Karkheck and G. Stell. Kinetic mean-field theories. *J. Chem. Phys.*, 75(3):1475–1487, 1981.

[23]K. Piechór. Non-local Korteweg stresses from kinetic theory point of view. *Arch. Mech.*, 60(1):23–58, 2008.

[24]M. Grmela. Kinetic equation approach to phase transitions. *J. Stat. Phys.*, 3(3):347–364, 1971.

[25]S. Takata and T. Noguchi. A simple kinetic model for the phase transition of the Van der Waals fluid. *J. Stat. Phys.*, 172(3):880–903, 2018.

[26]S. Takata, T. Matsumoto, A. Hirahara, and M. Hattori. Kinetic theory for a simple modeling of a phase transition: Dynamics out of local equilibrium. *Physical Review E*, 98(5):052123, 2018.

[27]E.S. Benilov and M.S. Benilov. Energy conservation and H theorem for the Enskog-Vlasov equation. *Phys. Rev. B*, 97(6):062115, 2018.

[28]E.S. Benilov and M.S. Benilov. Peculiar property of noble gases and its explanation through the Enskog–Vlasov model. *Physical Review E*, 99(1):012144, 2019.

[29]E.S. Benilov and M.S. Benilov. The Enskog–Vlasov equation: a kinetic model describing gas, liquid, and solid. *arXiv preprint arXiv:1812.06754*, 2018.

[30]A. Frezzotti. Boundary conditions at the vapor-liquid interface. *Phys. Fluids*, 23(3):030609, 2011.

[31]S. Fujikawa, T. Yano, and M. Watanabe. *Vapor-Liquid Interfaces, Bubbles and Droplets: Fundamentals and Applications*. Springer-Verlag, Heidelberg, 2011.

[32]A. Frezzotti and L. Gibelli. A kinetic model for equilibrium and non-equilibrium structure of the vapor-liquid interface. In *AIP Conference Proceedings*, volume 663, pages 980–987. AIP, 2003.

[33]A. Frezzotti, L. Gibelli, D. A. Lockerby, and J. E. Sprittles. Mean-field kinetic theory approach to evaporation of a binary liquid into vacuum. *Phys. Rev. Fluids*, 3(5):054001, 2018.

[34]M. Kon, K. Kobayashi, and M. Watanabe. Method of determining kinetic boundary conditions in net evaporation/condensation. *Phys. Fluids*, 26(7):072003, 2014.

[35]K. Kobayashi, K. Sasaki, M. Kon, H. Fujii, and M. Watanabe. Kinetic boundary conditions for vapor–gas binary mixture. *Microfluid. Nanofluid.*, 21(3):53, 2017.

[36]P. Barbante, A. Frezzotti, and L. Gibelli. A kinetic theory description of liquid menisci at the microscale. *Kinetic and Related Models*, 8(2):235–254, 2015.

[37]H. van Beijeren and M.H. Ernst. The modified Enskog equation. *Physica*, 68:437, 1973.

[38]N.F. Carnahan and K.E. Starling. Equation of state for nonattracting rigid spheres. *The Journal of Chemical Physics*, 51(2):635–636, 1969.

[39]R. Balescu. *Equilibrium and Nonequilibrium Statistical Mechanics*. John Wiley & Sons, New York, 1975.

[40]M.P. Allen and D.J. Tildesley. *Computer Simulation of Liquids*. Clarendon Press, 1989.

[41]K. Koura. Null-collision technique in the direct-simulation Monte Carlo method. *Physics of Fluids*, 29:3509–3511, November 1986.

[42]M. Shusser, T. Ytrehus, and D. Weihs. Kinetic theory analysis of explosive boiling of a liquid droplet. *Fluid. Dyn. Res.*, 27(6):353–365, 2000.

[43]S. S. Sazhin. Advanced models of fuel droplet heating and evaporation. *Prog. Energ. Combust.*, 32(2):162–214, 2006.

[44]S.I. Anisimov, D.O. Dunikov, V.V. Zhakhovskii, and S.P. Malyshenko. Properties of a liquid-gas interface at high-rate evaporation. *J. Chem. Phys.*, 110:8722–8729, 1999.

[45]R. Meland, A. Frezzotti, T. Ytrehus, and B. Hafskjold. Nonequilibrium molecular-dynamics simulation of net evaporation and net condensation, and evaluation of the gas-kinetic boundary condition at the interphase. *Phys. Fluids*, 16:223–243, 2004.

[46]T. Ytrehus. Theory and experiments on gas kinetics in evaporation. In J. Leith Potter, editor, *Rarefied gas dynamics: technical papers selected from the 10th International Symposium on Rarefied Gas Dynamics, Snowmass-at-Aspen, CO - July 1976*, volume 51 of *Progress in astronautics and aeronautics*, page 1197. American Institute of Aeronautics and Astronautics, 1977.

[47]P. Barbante and A. Frezzotti. A comparison of models for the evaporation of the Lennard-Jones fluid. *European Journal of Mechanics - B/Fluids*, 64.

[48]Y. Sone. Kinetic theoretical studies of the half-space problem of evaporation and condensation. *TTSP*, 29(3-5):227–260, 2000.

[49]H. Struchtrup, A. Beckmann, A. S. Rana, and A. Frezzotti. Evaporation boundary conditions for the R13 equations of rarefied gas dynamics. *Physics of Fluids*, 29(9):092004, 2017.

[50]J. W. Cipolla, H. Lang, and S. K. Loyalka. Kinetic theory of condensation and evaporation. ii. *The Journal of Chemical Physics*, 61(1):69–77, 1974.

[51]Y. Sone, K. Aoki, H. Sugimoto, and T. Yamada. Steady evaporation and condensation on a plane condensed phase. *Theor. Appl. Mech.*, 3:89–93, 1988.

[52]A. Frezzotti. Kinetic theory description of the evaporation of multi-component substances. In Ching Shen, editor, *Rarefied Gas Dynamics, Proceedings of the 20th International Symposium, 19-23 August 1996, Beijing, China*, pages 837–846, Beijing, China, 1997. Peking University Press.

[53]A. Frezzotti. A numerical investigation of the steady evaporation of a polyatomic gas. *European Journal of Mechanics - B/Fluids*, 26(1):93–104, 2007.

[54]T. Soga. A kinetic theory analysis of evaporation and condensation of a diatomic gas. *Phys. Fluids*, 28:1280–1285, 1985.

[55]Y. Shi, G. H. Tang, H. F. Lin, P. X. Zhao, and L. H. Cheng. Dynamics of droplet and liquid layer penetration in three-dimensional porous media: A lattice Boltzmann study. *Physics of Fluids*, 31(4):042106, 2019.

[56]G. Castanet, O. Caballina, and F. Lemoine. Drop spreading at the impact in the Leidenfrost boiling. *Physics of Fluids*, 27(6):063302, 2015.